




# PHOTONICS Research

## Regrowth-free AlGaInAs MQW polarization controller integrated with a sidewall grating DFB laser

XIAO SUN,<sup>1,\*</sup>  SONG LIANG,<sup>2</sup> WEIQING CHENG,<sup>1</sup> SHENGWEI YE,<sup>1</sup> YIMING SUN,<sup>1</sup> YONGGUANG HUANG,<sup>2</sup> RUIKANG ZHANG,<sup>2</sup> JICHUAN XIONG,<sup>3</sup>  XUEFENG LIU,<sup>3</sup> JOHN H. MARSH,<sup>1</sup>  AND LIANPING HOU<sup>1</sup> 

<sup>1</sup>James Watt School of Engineering, University of Glasgow, Glasgow G12 8QQ, UK

<sup>2</sup>Institute of Semiconductors, Chinese Academy of Sciences, Beijing 100083, China

<sup>3</sup>School of Electronic and Optical Engineering, Nanjing University of Science and Technology, Nanjing 210094, China

\*Corresponding author: x.sun.2@research.gla.ac.uk

Received 21 November 2022; accepted 11 February 2023; posted 13 February 2023 (Doc. ID 480676); published 30 March 2023

Polarization control is at the heart of high-capacity data optical communication systems, such as polarization-division multiplexers and Stokes vector modulation transmitters. Despite passive polarization control being mature, the realization of monolithically integrated polarization controllers and single longitudinal mode light sources, such as distributed-feedback (DFB) lasers, is of importance. In this research, we report an AlGaInAs multiple-quantum-well photonic integrated circuit device which can control the state of polarization of the output light source, consisting of a polarization mode converter (PMC), a differential phase shifter (DPS), and a sidewall grating DFB laser. We demonstrate an asymmetrical stepped-height ridge waveguide PMC to realize TE to TM polarization conversion and a symmetrical straight waveguide DPS to enable polarization rotation from approximately counterclockwise circular polarization to linear polarization. Based on the identical epitaxial layer scheme, all the PMC, DPS, and DFB lasers can be integrated monolithically using only a single step of metalorganic vapor-phase epitaxy and two steps of III-V material dry etching. For the DFB-PMC device, a high TE to TM polarization conversion efficiency (98.4%) over a wide range of DFB injection currents is reported at 1555 nm wavelength. For the DFB-PMC-DPS device, a nearly 60° rotation of the Stokes vector on the Poincaré sphere was obtained with a range of bias voltage from 0 to -3.0 V at a laser drive current of 170 mA.

Published by Chinese Laser Press under the terms of the [Creative Commons Attribution 4.0 License](https://creativecommons.org/licenses/by/4.0/). Further distribution of this work must maintain attribution to the author(s) and the published article's title, journal citation, and DOI.

<https://doi.org/10.1364/PRJ.480676>

### 1. INTRODUCTION

The ability to control the polarization state is of substantial interest in optical communication systems such as those using high-speed complex digital signal processing to manipulate the TE-TM polarization state of light [1] or Stokes vector modulation and direct detection systems [2,3]. For these applications, there is a growing interest in integrating a polarization controller with the light source, the detectors, and other components in a photonic integrated circuit (PIC). As an increasing number of devices such as laser diodes (LDs) [4] and electro-absorption modulators [5] utilize multiple-quantum-well (MQW) structures as the active region, it is desirable to design a polarization controller compatible with MQW structures.

Several different material systems and designs have been proposed for polarization controllers including the silicon-on-insulator platform [6], the InGaAlAs/InP platform [5],

and the InGaAsP/InP platform [7,8]. A typical waveguide polarization converter comprises a cascade of polarization mode converters (PMCs) and MQW polarization-dependent phase shifters (PD-PSs) [5,9] to achieve an arbitrary state of polarization (SOP). The light source can be an external LD or a monolithically integrated laser [4,10]. However, many reported PMCs utilize bulk material as the core layer in the waveguide to achieve a high polarization conversion efficiency (PCE) at a short waveguide length. This approach requires relatively complicated regrown butt-joint PIC techniques to integrate a bulk PMC with an MQW-based PD-PS. In Ref. [9], a passive bulk PMC was monolithically integrated with an active MQW-based PD-PS by using the butt-joint technique and was a demonstrator of an efficient polarization controller in the InGaAsP/InP material system; however, the device had no monolithic LD. In Ref. [3], an MQW-based PMC was monolithically

integrated with an MQW-based Fabry–Perot (FP) LD using the identical epitaxial layer (IEL) integration scheme, but the PCE was limited, being only 80% in Refs. [4,11] and around 50%–68% in Ref. [9]. Until now there is no report of a PMC integrated with a distributed-feedback (DFB) laser.

The crucial issue for integrating PMCs with MQW devices is the inherent birefringence of the MQW, which disturbs the optimal rotation of the SOP. The two main mechanisms of SOP conversion are the mode-evolution method [12], which utilizes the shifting of the propagating mode inside the waveguide, and the mode coupling method [8], which exploits the beating between two eigenmodes to enable polarization rotation along the PMC waveguide. Because mode coupling PMCs enable polarization conversion within a short length of waveguide, it is important to reduce the absorption loss caused by the inter-band exciton transitions inside an MQW-based PMC monolithically integrated with an MQW-based LD [13]. To realize good mode-matching between the waveguides of monolithic PMCs and LDs, we have proposed an AlGaInAs/InP MQW-based sidewall grating (SWG) DFB laser monolithically integrated with a stepped height waveguide PMC [14]. A novel MQW-based epitaxial structure was designed and optimized for both the PMC and SWG DFB laser through a series of full-wave simulations. In this work, based on our simulation work an AlGaInAs MQW SWG DFB laser was fabricated and monolithically integrated with both a stepped waveguide PMC and a differential phase shifter (DPS) based on the IEL integration scheme, for the first time. This approach needs only a single step of metalorganic vapor-phase epitaxy (MOVPE) and two steps of III-V material dry etching. The monolithic DFB-PMC and DFB-PMC-DPS devices reported here avoid the complicated etch and regrowth processes required for conventional buried grating DFB laser structures and time-consuming butt-joint or selective area growth PIC technologies. The DFB-PMC device has a high TE to TM PCE (98.4%) over a wide range of DFB injection currents ( $I_{\text{DFB}}$ ) at an operating wavelength of 1555 nm. For the DFB-PMC-DPS device, a rotation of nearly 60° of the Stokes vector (SV) was obtained on the Poincaré sphere with a range of bias voltage from 0 to -3.0 V and  $I_{\text{DFB}} = 170$  mA.

## 2. DEVICE DESIGN AND FABRICATION

The wafer structure used for the DFB-PMC and DFB-PMC-DPS is the same as that described in Ref. [14]. The wafer was grown on an InP substrate by MOVPE. The room temperature photoluminescence (PL) peak of the QWs was located at a wavelength of 1530 nm. An optimized 300 nm thick 1.25Q layer (1.25Q means the room temperature PL peak of this material is at 1.25  $\mu\text{m}$ ) is embedded below the MQW to increase the difference between the propagation constants of the  $\text{TE}_0$  and  $\text{TM}_0$  fundamental transverse modes of the PMC to reduce the half-beat length ( $L_\pi$ ) and increase the PCE. The optical confinement factor of the QWs is 9%. Two kinds of polarization controllers—DFB-PMC and DFB-PMC-DPS—are proposed and are shown in Fig. 1(a). Both devices contain the same 1200  $\mu\text{m}$  long SWG ridge DFB laser. The ridge waveguide of DFB is 2.5  $\mu\text{m}$  wide and 1.92  $\mu\text{m}$  high. The gratings are of first order with a 50% duty cycle, formed by etching

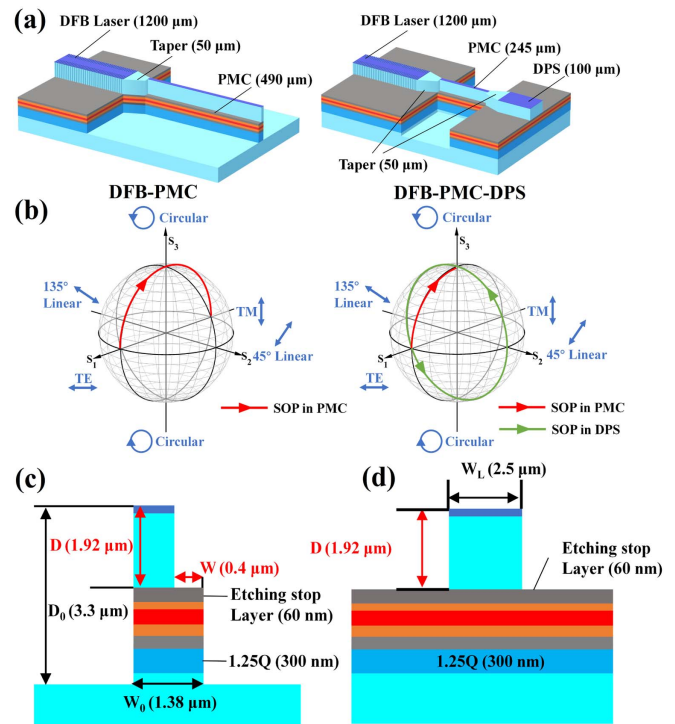


**Fig. 1.** (a) Schematic of the monolithic DFB-PMC device (left) and DFB-PMC-DPS device (right); (b) SV propagates inside the DFB-PMC (left) and the DFB-PMC-DPS device (right); (c) cross-section structure of the PMC; (d) cross-section structure of the DPS.

0.6  $\mu\text{m}$  depth into the sidewalls of the waveguide, as shown in Fig. 1(a). For the DFB-PMC device, LDs with three different Bragg wavelengths were designed and fabricated. The grating period is 238 nm for a 1550 nm Bragg wavelength, 236.5 nm for a 1540 nm Bragg wavelength, and 240.3 nm for a 1565 nm Bragg wavelength. A quarter-wavelength shift section was inserted at the center of the DFB laser cavity to ensure single longitudinal mode (SLM) oscillation. The lengths of the PMCs in the DFB-PMC and DFB-PMC-DPS are 490  $\mu\text{m}$  and 245  $\mu\text{m}$ , respectively. The PMC is connected to the DFB LD using a 50  $\mu\text{m}$  long taper for the DFB-PMC device and is connected to the DFB laser and DPS, respectively, by two 50  $\mu\text{m}$  long tapers for the DFB-PMC-DPS device. The width of the taper is changed from 2.5 to 1.38  $\mu\text{m}$  to facilitate the TE mode transition to the PMC and prevent the generation of multiple transverse modes. The simulated reflection coefficient between the shallow etched DFB and deeply etched taper sections is about  $7 \times 10^{-6}$ , which has a negligible effect on the DFB performance. The simulated taper excess optical loss is 1%, i.e., 0.044 dB, which includes the scattering and mode mismatch loss and can also be neglected. Figure 1(b) presents the SV rotation inside those two devices. For the DFB-PMC device, the SV rotates around the  $S_2$  axis arriving at the  $S_1 - S_2$  plane where the output mode is TM-polarized. For the DFB-PMC-DPS device, after the PMC, the SV rotates around the  $S_2$  axis (red line) close to the north pole, corresponding to counter-clockwise circular polarization. The SV is then rotated around the  $S_1$  axis within the  $S_2 - S_3$  plane by using the reverse biased DPS section (green line). Assuming a TE-polarized input

[ $S = (1, 0, 0)$ ], the variation of  $S = (S_1, S_2, S_3)^T$  and the PCE inside the PMC waveguide can be found from [15,16]

$$S = \begin{pmatrix} S_1 \\ S_2 \\ S_3 \end{pmatrix} = \begin{pmatrix} 1 - 2 \sin^2(2\varphi) \sin^2\left(\pi \frac{L_{\text{PMC}}}{2L_\pi}\right) \\ \sin(4\varphi) \sin\left(\pi \frac{L_{\text{PMC}}}{2L_\pi}\right) \\ \sin(2\varphi) \sin\left(\pi \frac{L_{\text{PMC}}}{L_\pi}\right) \end{pmatrix}, \quad (1)$$

$$\text{PCE} = \sin^2(2\varphi) \sin^2\left(\pi \frac{L_{\text{PMC}}}{2L_\pi}\right) = \frac{1 - S_1}{2} \times 100\%, \quad (2)$$

where  $\varphi$  is the rotated angle of the eigenmodes in the PMC waveguide, and  $L_{\text{PMC}}$  is the length of the PMC. In this work  $L_{\text{PMC}}$  is equal to the half-beat length  $L_\pi = \pi/(\beta_1 - \beta_2)$ , where  $\beta_1$  and  $\beta_2$  are the propagation constants of the  $\text{TE}_0$  and  $\text{TM}_0$  eigenmodes in the PMC waveguide. To realize the SV rotation in Fig. 1(b), the value of  $\varphi$  should be  $45^\circ$  and  $L_{\text{PMC}}$  should be equal to  $L_\pi$  for the DFB-PMC and equal to  $L_\pi/2$  for the DFB-PMC-DPS. The dimensions of the stepped-height PMC waveguide chosen here are  $W_0 = 1.38 \mu\text{m}$ ,  $W = 0.4 \mu\text{m}$ ,  $D_0 = 3.3 \mu\text{m}$ , and  $D = 1.92 \mu\text{m}$ , as shown in Fig. 1(c).  $D$  can be precisely controlled because the top 60 nm thick AlGaInAs waveguide layer acts as a dry etch stop layer when using a  $\text{CH}_4/\text{H}_2/\text{O}_2$  inductively coupled plasma (ICP) recipe. Figure 1(d) presents the cross section of the DPS, which is a symmetric, shallow etched ridge waveguide with a width of  $2.5 \mu\text{m}$  and height of  $1.92 \mu\text{m}$ , the same as that of the DFB section. Figures 2(a) and 2(b) present the fundamental mode profiles in the taper output section and PMC waveguide. The PMC eigenmode is optimized to rotate the electric/magnetic fields through  $45^\circ$ . After propagating a half-beat length  $L_\pi$ , the SV is rotated  $180^\circ$  around the  $S_2$  axis as found from

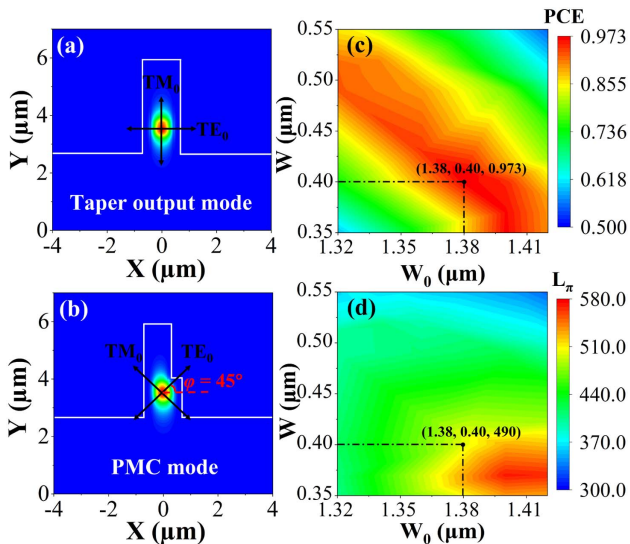


**Fig. 2.** (a), (b) The fundamental eigenmodes in taper output (a) and PMC stepped-height ridge waveguide (b); (c) and (d) calculated maximum PCE (c), and corresponding  $L_\pi$  (d) as a function of waveguide width ( $W_0$ ) and corner width ( $W$ ) at an operating wavelength of 1550 nm.

Eq. (1), and the output becomes purely TM-polarized. Hence, to optimize the PCE and  $L_\pi$  of the PMC waveguide, a full-wave simulation was made using an FDTD software package. The input light wavelength was set at 1550 nm. The calculated effective modal indices ( $N_{\text{eff}}$ ) of the fundamental TE and TM modes are 3.21109 and 3.20951, respectively. Figures 2(c) and 2(d) show contour plots of the calculated PCE and  $L_\pi$  as a function of  $W_0$  and  $W$  at the operating wavelength of 1550 nm. The final optimum widths of the PMC waveguide are  $W_0 = 1.38 \mu\text{m}$  and  $W = 0.4 \mu\text{m}$ , which provide a high PCE (97.3%) and short  $L_\pi$  (490  $\mu\text{m}$ ).

In the DPS waveguide, via the band-filling effect (forward bias) or quantum-confined Stark effect (QCSE) (reverse bias), the phase shift between  $\text{TE}_0$  mode and  $\text{TM}_0$  mode in the DPS can be tuned because the phase modulation efficiency generally differs for the  $\text{TE}_0$  and  $\text{TM}_0$  modes. The SV rotation angle  $\Delta\theta$  in the DPS can therefore be controlled by the bias voltage [15]. DPSs based on the QCSE have picosecond switching speeds and are faster than those based on the band-filling effect which have nanosecond switching speeds [17], although measurement of the switching speed is beyond the scope of this paper. Reverse bias operation of the DPS is therefore preferred and was used to change the rotation angle  $\Delta\theta$ , which can be calculated from

$$\Delta\theta = (\Delta\beta_{\text{TE}} - \Delta\beta_{\text{TM}}) \times L_{\text{DPS}} = \frac{2\pi L_{\text{DPS}}}{\lambda} (\Delta n_{\text{TE}} - \Delta n_{\text{TM}}), \quad (3)$$

where  $\Delta n_{\text{TE}}$  and  $\Delta n_{\text{TM}}$  are the changes of the refractive index of the  $\text{TE}_0$  and  $\text{TM}_0$  modes, respectively, and are determined from the change in absorption coefficient ( $\Delta\alpha$ ) using the Kramers–Krönig relationship [18]:

$$\Delta n(E) = \frac{c\hbar}{\pi} \int_0^\infty \frac{\Delta\alpha(E')}{E'^2 - E^2} dE', \quad (4)$$

where  $E$  is the photon energy,  $\hbar$  is Planck's constant divided by  $2\pi$ , and the total absorption coefficient,  $\alpha$ , is the sum of the absorption coefficient of the exciton resonance in the quantum well ( $\alpha_{\text{ex}}$ ) and the absorption coefficient between the conduction and valence band transition ( $\alpha_{\text{con}}$ ). They are expressed as [19]

$$\alpha_{\text{ex}} = \sum_{i,j} \frac{4e^2 |p_{\text{cv}}|^2}{\epsilon_0 c n m_0^2 E_{\text{ex}(i,j)} \lambda_{\text{ex}(i,j)}^2 L_z} |\langle \chi_{\text{ci}} | \chi_{\text{vi}} \rangle|^2 B(\omega - E_{\text{ex}(i,j)}), \quad (5)$$

$$\alpha_{\text{con}} = \frac{\mu e^2 |p_{\text{cv}}|^2}{\epsilon_0 c n m_0^2 2\omega L_z} \sum_{i,j} |\langle \chi_{\text{ci}} | \chi_{\text{vi}} \rangle|^2 \times \int_{E_{\text{cv}(i,j)}}^\infty S(E, E_{\text{cv}(i,j)}) L(E, \omega) dE, \quad (6)$$

$$\alpha = \alpha_{\text{ex}} + \alpha_{\text{con}}, \quad (7)$$

where  $\chi_{\text{ci}}$  and  $\chi_{\text{vi}}$  are the envelope wave functions of conduction and valence bands, respectively,  $n$  is the refractive index,  $c$  is the velocity of light in vacuum,  $\epsilon_0$  is the permittivity of free space, and  $L_z$  is the as-grown QW width.  $S$  is the Sommerfeld enhancement factor,  $L$  is the Lorentzian broadening factor, and



$p_{cv}$  is the optical matrix element at the band edge. The parameters used here to calculate  $\alpha$  are referenced in Ref. [20]. Figure 3(a) shows the calculated TE and TM absorption coefficients as a function of wavelength with  $V_{DPS}$  at 0 V and -3 V, respectively. The modal absorption coefficient for the TE mode at 1.55  $\mu\text{m}$  wavelength is about  $9.76 \text{ cm}^{-1}$  and the TM mode absorption coefficient is  $2.6 \text{ cm}^{-1}$  at 0 V bias voltage. The TE modal absorption coefficient of  $9.76 \text{ cm}^{-1}$  fits very well with our measured result of  $9 \pm 1 \text{ cm}^{-1}$ , as discussed in Section 3. As  $|V_{DPS}|$  is increased, there is a redshift of the exciton peak. It is also found that the absorption coefficient at -3 V bias voltage is high ( $500 \text{ cm}^{-1}$ ), which means the DPS cannot be too long. Here a 100  $\mu\text{m}$  length DPS was used, and 22 dB absorption loss at -3 V bias was produced, the same as the measured one. Figure 3(b) presents the difference of the effective refractive index changes between the TE and TM modes ( $\Delta n_{TE} - \Delta n_{TM}$ ) for different  $V_{DPS}$ . The calculated  $\Delta\theta$  as a function of  $V_{DPS}$  at 1.557  $\mu\text{m}$  wavelength is presented in Fig. 3(c), with a predicted  $71^\circ$  phase shift at  $V_{DPS} = -3.0 \text{ V}$ .

The DFB-PMC device fabrication processes are presented in Fig. 4. The wafer was grown on an InP substrate by MOVPE [Fig. 4(a)]. The DFB grating and PMC first step waveguide pattern were defined by electron-beam lithography (EBL). Negative tone hydrogen silsesquioxane (HSQ) was used as the EBL resist hard mask for ICP dry etching, as shown in Fig. 4(b). Figure 4(c) shows the shallow etched ridge, which took place in two stages. The ridge was first etched to a depth of 1.89  $\mu\text{m}$  in an ICP dry etch tool using a  $\text{Cl}_2/\text{CH}_4/\text{H}_2/\text{Ar}$  gas mixture, the average etch rate for InP and InGaAsP being about 183 nm/min, and then the gas recipe was changed to  $\text{CH}_4/\text{H}_2/\text{O}_2$ , to etch the ridge to a final depth of 1.92  $\mu\text{m}$ . This could be stopped on the AlGaInAs layer, as the average etch rate of InP/InGaAsP was about 78 nm/min, and that of AlGaInAs was 3 nm/s, achieving 26-fold selectivity. After the shallow etch, both the DFB section and the top and one side of the PMC were protected by HSQ defined by EBL, as

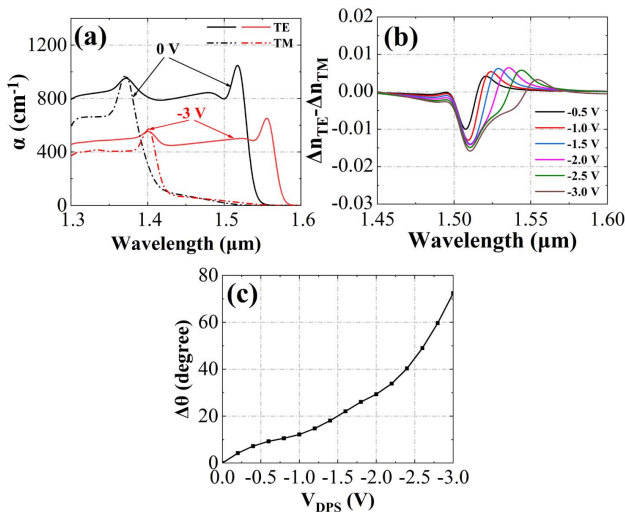


**Fig. 3.** (a) Calculated TE and TM absorption coefficients in the DPS. (b) The difference of the effective refractive index changes between the TE and TM modes at different  $V_{DPS}$ . (c) Phase-shifted angle as a function of  $V_{DPS}$  at 1.557  $\mu\text{m}$  operation wavelength.

shown in Fig. 4(d). A second stage of  $\text{Cl}_2/\text{CH}_4/\text{H}_2/\text{Ar}$  ICP etching was then used to etch one side of the PMC waveguide to a depth of 3.3  $\mu\text{m}$  [Fig. 4(e)]. Finally, all HSQ was removed by HF acid, as shown in Fig. 4(f). The fabrication workflow is depicted in Fig. 4(g); only a single step of MOVPE and two steps of III-V material dry etching are required for the whole integrated device. Scanning electron microscope (SEM) images of the PMC waveguide after the first shallow etch, second step EBL, and deep etch are shown in Figs. 4(h), 4(i), and 4(j), respectively. The subsequent deposition of  $\text{SiO}_2$  and HSQ passivation layers,  $\text{SiO}_2$  window opening, P-contact deposition, substrate thinning, and N-contact deposition were the same as for conventional LD fabrication [21]. SEM images of the DFB grating, output facet of the PMC, and DFB-PMC device are presented in Figs. 5(a)–5(c). The optical microscope pictures of the completed DFB-PMC and DFB-PMC-DPS devices are depicted in Figs. 5(d) and 5(e), respectively. Finally, the devices were mounted epilayer up on a copper heat sink on a Peltier

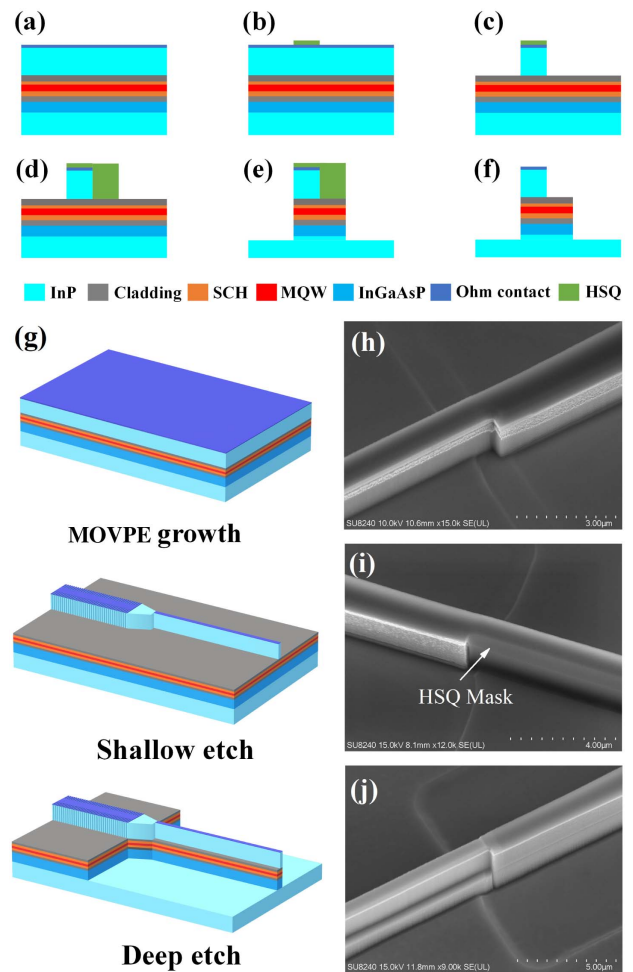


**Fig. 4.** (a)–(f) Fabrication procedures: (a) MOVPE epilayer growth, (b) EBL to define the laser and PMC first step waveguide, (c) ICP shallow etching, (d) EBL to define the second step waveguide of the PMC, (e) ICP deep etching, (f) HSQ elimination. (g) Workflow of monolithic DFB-PMC device fabrication. (h)–(j) SEM images after (h) the first shallow etch, (i) second step EBL using HSQ photoresist, (j) PMC deep etch and HSQ elimination.

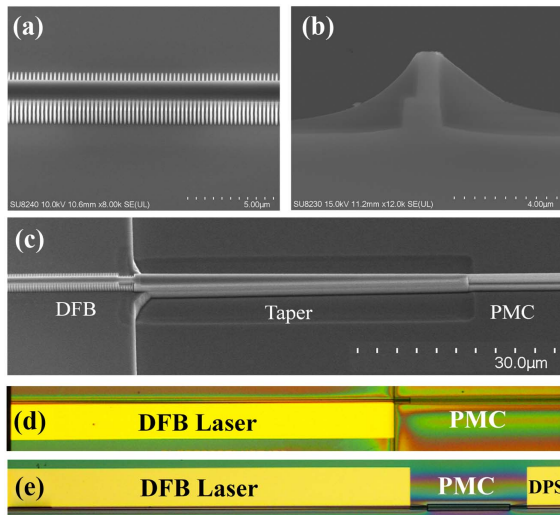


**Fig. 5.** (a)–(c) SEM images of (a) the DFB laser with sidewall gratings, (b) output facet of the PMC, (c) DFB-PMC device. (d) and (e) Microscope pictures of the (d) DFB-PMC device and (e) DFB-PMC-DPS device.

cooler. The heat sink temperature was set at 20°C and the devices were tested under CW conditions.

For the DFB-PMC-DPS device, the fabrication process is the same as that of the DFB-PMC devices and will not be discussed in further detail.

### 3. DEVICE MEASUREMENT

#### A. DFB-PMC Device

As described above, for the DFB-PMC device, DFBs were fabricated with three Bragg wavelengths, i.e., 1540, 1550, and 1565 nm. Figure 6 shows their optical spectra at specific injection DFB currents ( $I_{\text{DFB}}$ ) and 2D optical spectra as a function of  $I_{\text{DFB}}$  from the DFB rear side and PMC side, respectively. All spectra were measured with a resolution bandwidth of 0.06 nm. The measurement results of wavelength, single-mode suppression ratios (SMSRs), and average current-induced wavelength redshift coefficient (ACWRC) are listed in Table 1. The

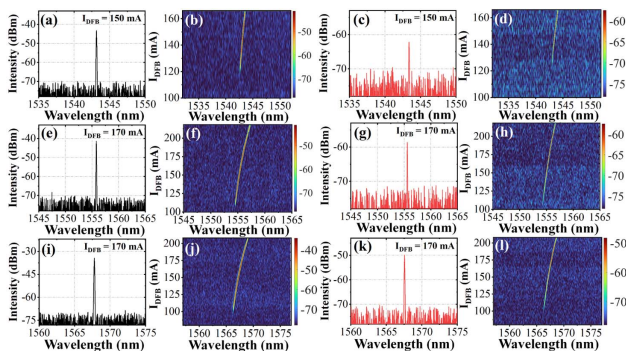


**Fig. 6.** (a)–(d) Measured optical spectra for the 1543 nm DFB-PMC device measured from DFB (a), (b) and PMC (c), (d) facets. (e)–(h) Optical spectra for the 1555 nm DFB-PMC device from DFB (e), (f) and PMC (g), (h) facets. (i)–(l) Optical spectra for the 1567 nm DFB-PMC device from DFB (i), (j) and PMC (k), (l) facets.

measured wavelengths of the DFB lasers with designed operation wavelengths of 1540 nm, 1550 nm, and 1565 nm are 1543.6 nm, 1555.8 nm, and 1568.2 nm, with  $I_{\text{DFB}}$  set at 150 mA, 170 mA, and 170 mA, respectively. Compared to the designed Bragg wavelengths, the measured wavelengths are slightly redshifted due to the heating effect. The corresponding SMSRs measured from the DFB rear facet are 27 dB, 29 dB, and 38 dB, respectively. At the PMC output facet, the SMSRs were reduced to 8 dB, 12 dB, and 20 dB. This is due to the significant inter-band and exciton absorption inside the PMC waveguide when the propagating light wavelength is close to the PL wavelength (1530 nm) of the MQW core. The measured ACWRCs from the DFB and PMC sides are 0.025 nm/mA, 0.0207 nm/mA, and 0.0271 nm/mA for Bragg grating wavelengths at 1540 nm, 1550 nm, and 1565 nm, respectively, all exhibiting stable SLM operation. To estimate the internal loss in the PMC waveguide, an 800  $\mu\text{m}$  length FP laser was fabricated in the same wafer and fabrication run, and the internal loss in the waveguide was  $9 \pm 1 \text{ cm}^{-1}$  measured by the Haki–Paoli method [shown in Fig. 7(a)]. To estimate the  $\kappa$  value of the DFB lasers, an 800  $\mu\text{m}$  long DFB laser with a Bragg wavelength of 1565 nm and a  $\pi$ -phase shift section inserted at the center of the cavity was also fabricated. Figure 7(b) shows the optical spectrum at the threshold current (48 mA). The measured central wavelength is 1566.5 nm, and the stop band width ( $\Delta\lambda_s$ ) is 1.14 nm. The grating coupling coefficient  $\kappa$  can be estimated using [22]

$$\kappa = n_{\text{eff}} \frac{\Delta\lambda_s}{\lambda_B^2}, \quad (8)$$

where  $n_{\text{eff}}$  is the effective index (3.26);  $\lambda_B$  is the lasing wavelength of the DFB laser. The  $\kappa$  of the fabricated grating is estimated to be  $\sim 15 \text{ cm}^{-1}$ , and  $\kappa L = 1.8$  for the 1200  $\mu\text{m}$  length DFB laser, which ensures stable SLM operation.

The setup for the SOP measurement is shown in Fig. 8. Devices were mounted on a thermoelectric cooler and the temperature was controlled at 20°C as stated previously. The output light from the PMC was coupled into a lensed polarization-maintaining fiber and transmitted to a polarimeter to measure the SOP. Both the current driver and the polarimeter were controlled by a computer through the general-purpose bus interface by LabVIEW software. We first measured the SOP at the DFB laser rear facet at  $I_{\text{DFB}}$  from 104 to 210 mA, and the SV was constant at (0.998, 0.05, 0.04). Figures 9(a)–9(c) present the SV at the PMC facets of DFB-PMC devices with different Bragg wavelengths. The PCE was calculated from Eq. (2) and the values are listed in Table 2. For the DFB-PMC device with a designed Bragg wavelength at 1550 nm, the average  $S_1$  parameter was  $-0.968$  representing a PCE of 98.4% for  $140 \text{ mA} < I_{\text{DFB}} < 190 \text{ mA}$  (corresponding wavelength range 1554.9–1555.9 nm). The maximum PCE was 99.1% measured at  $I_{\text{DFB}} = 180 \text{ mA}$ . The deviation of the measured PCE is due to the measurement errors caused by the noise of the DC source driving the DFB laser, and environmental influences such as temperature fluctuations and mechanical vibration. For the DFB-PMC device with a designed Bragg wavelength at 1540 nm, the average PCE over the wavelength range from 1543.6 to 1544.2 nm was found to be 93% for  $150 \text{ mA} < I_{\text{DFB}} < 170 \text{ mA}$  and the maximum

**Table 1. Measured Parameters of the Three DFB-PMC Devices with Different Designed Bragg Wavelengths**

Designed Bragg Grating Wavelength (nm)	DFB Facet SMSR (dB)	PMC Facet SMSR (dB)	Measured Current (mA) and Wavelength Range (nm)	ACWRC (nm/mA)
1540	27	8	Current: 118–170 Wavelength: 1542.9–1544.2	0.0250
1550	29	12	Current: 104–220 Wavelength: 1554.2–1556.6	0.0207
1565	38	20	Current: 97–211 Wavelength: 1566.3–1569.4	0.0271

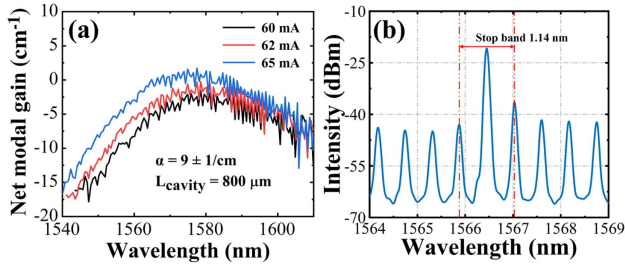


**Fig. 7.** (a) Measured net modal gain as a function of the wavelength using the Haki–Paoli method, (b) optical spectrum at threshold current (48 mA) of a 800  $\mu\text{m}$  length DFB LD with a  $\pi$ -phase shift section inserted at the center of the DFB LD cavity.

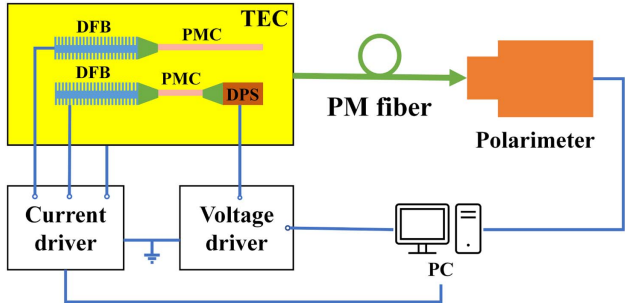


**Fig. 8.** Experimental setup for the SOP measurement for DFB-PMC and DFB-PMC-DPS devices.

PCE was found to be 94.3% at  $I_{\text{DFB}} = 162$  mA. For the DFB-PMC device with a designed Bragg wavelength at 1565 nm, the average PCE was 89.8% over the range  $140 \text{ mA} < I_{\text{DFB}} < 190$  mA and wavelength from 1567.4 to 1568.7 nm. The maximum PCE was 90.5% (at  $I_{\text{DFB}} = 174$  mA). Figure 10 presents a comparison between the calculated PCE from the full-wave simulation and the measured average PCE as a function of wavelength. There is very good agreement between the simulated and measured results.

**B. DFB-PMC-DPS Device**

In light of the performance of the DFB-PMC devices, the DFB-PMC-DPS devices were fabricated with a Bragg grating wavelength at 1550 nm. Figure 11 shows the optical spectra measured from the rear side of the DFB section and from the DPS output section with  $V_{\text{DPS}} = 0$  V. The peak lasing wavelength is at 1557.2 nm with an SMSR of 35 dB at the

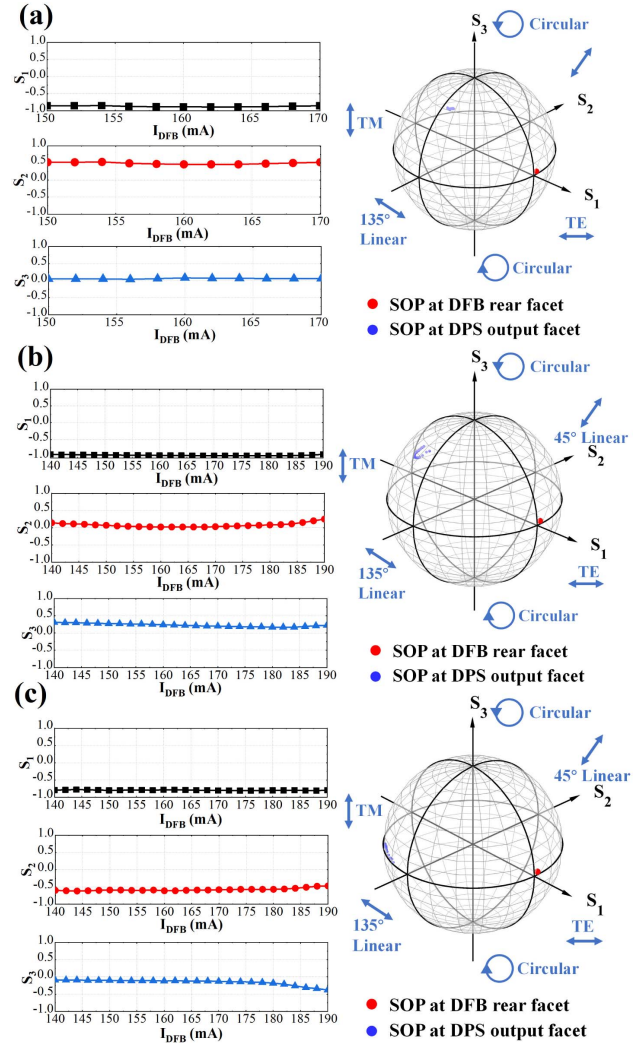


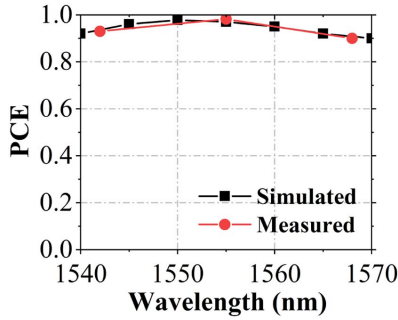
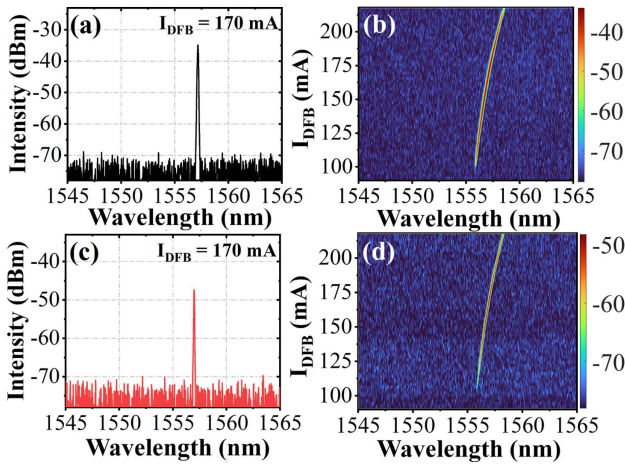
**Fig. 9.** Measured SV at the PMC side for (a) 1543 nm, (b) 1555 nm, (c) 1568 nm wavelength DFB-PMC devices.

DFB facet for  $I_{\text{DFB}} = 170$  mA, and the ACWRC is 0.023 nm/mA. We first measured the SV at the DPS output facet with  $V_{\text{DPS}} = 0$  V, as shown in Fig. 12(a). The SV lies near (0.05, 0.5, 0.865) for the range of  $I_{\text{DFB}}$  from 160 to 175 mA. This is a small deviation from a pure counterclockwise circular polarization state and is due to the birefringence of the taper and DPS waveguide. Then  $I_{\text{DFB}}$  was fixed at 170 mA and  $V_{\text{DPS}}$  was gradually changed from 0 to  $-3$  V. The SV measured at the DPS output facet is depicted in Fig. 12(b). It is found



**Table 2.** Measured PCE from the PMC Side of the DFB-PMC Devices

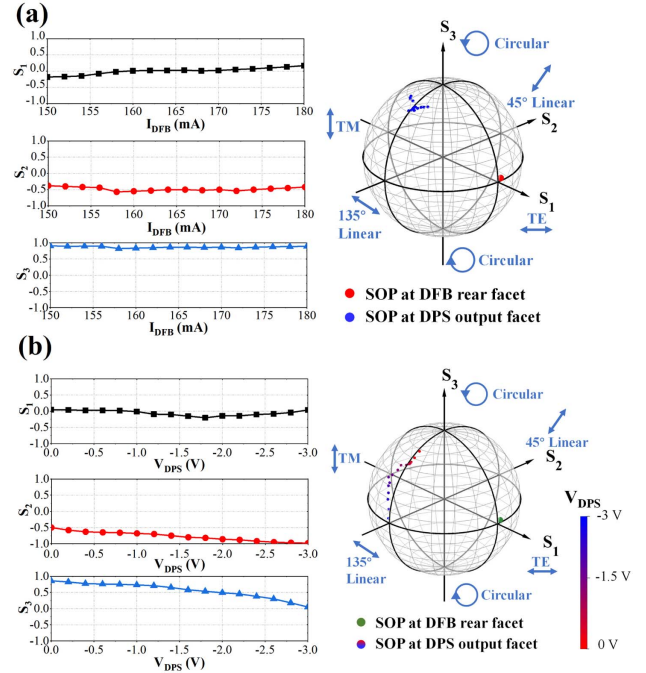
Designed DFB Laser Wavelength (nm)	Measured DFB Laser Wavelength (nm)	Current Range (mA)	Average PCE	MAX PCE
1540	1543.6–1544.2	150–170	93.0%	94.3%
1550	1554.9–1555.9	140–190	98.4%	99.1%
1565	1567.4–1568.7	140–190	89.8%	90.5%

**Fig. 10.** Simulated and measured PCE versus DFB lasing wavelength.**Fig. 11.** Measured optical spectrum from (a), (b) DFB LD rear facet and (c), (d) DPS section output facet.

that the SV rotates along the  $S_2 - S_3$  plane, and the measured rotation angle  $\Delta\theta$  as a function of  $V_{DPS}$  is presented in Fig. 13 along with the calculated result from Fig. 3(c). A phase shift of nearly  $60^\circ$  is seen as  $V_{DPS}$  is changed from 0 to  $-3.0$  V in steps of  $-0.2$  V. When  $V_{DPS}$  is changed from 0 to  $-2.2$  V, the measured and simulated values fit very well. When  $|V_{DPS}| > 2.2$  V, the deviations between them increase, which may be due to measurement errors because the output power from the DPS is low and the measurement accuracy is reduced.

#### 4. DISCUSSION

Here the reported rotation angle in the DPS is limited because the DPS is only  $100 \mu\text{m}$  long. To increase the output power

**Fig. 12.** (a) Measurement of SV at the DPS side as a function of  $I_{DFB}$  with  $V_{DPS} = 0$  V, (b) rotation of SV at the DPS output facet as a function of  $V_{DPS}$  for DFB-PMC-DPS devices with  $I_{DFB} = 170$  mA.

from the PMC or DPS side of the devices and improve the SV rotation performance in the DPS, quantum well intermixing (QWI) could be used to blueshift the bandgap in the PMC and DPS sections and reduce their absorption loss. In Ref. [13], we have proposed a PMC device with a  $100$  nm blueshift by QWI; the degree of intermixing  $N(z, L_D)$  is represented by the diffusion length ( $L_D$ ) on the group III substance as

$$N(z, L_D) = (N_W - N_B) \left[ 1 - \frac{1}{2} \operatorname{erf} \left( \frac{z - \frac{L_W}{2}}{2L_D} \right) + \frac{1}{2} \operatorname{erf} \left( \frac{z + \frac{L_W}{2}}{2L_D} \right) \right], \quad (9)$$

where  $N_W$  and  $N_B$  are the initial atomic mole fractions for QW and QB materials, respectively,  $z$  is the quantization direction along the growth axis (QW centered at  $z = 0$ ), “erf” denotes the error function, and  $L_W$  is the QW width. For the  $100$  nm blueshift,  $L_D$  is calculated to be  $1.53$  nm. As reported in Ref. [13], the TE and TM absorption coefficients in the DPS with a  $100$  nm blueshift by QWI can also be calculated using Eqs. (5)–(7) and are presented in Fig. 14(a). The modal absorption losses at  $1.55 \mu\text{m}$  are about  $4.75 \text{ cm}^{-1}$  and

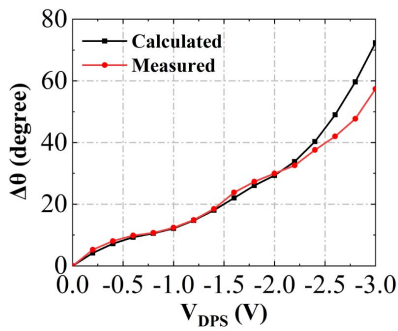


**Fig. 13.** Comparison between the measured and simulated phase shift angles as a function of  $V_{\text{DPS}}$ .

$2.3 \text{ cm}^{-1}$  for the TE and TM modes, respectively, for  $V_{\text{DPS}}$  at both 0 V and  $-3 \text{ V}$ , which are close to the measured results, i.e.,  $4.5 \pm 0.5 \text{ cm}^{-1}$  for TE and  $2.0 \pm 0.3 \text{ cm}^{-1}$  for TM [23]. Therefore, after QWI, applying a high  $V_{\text{DPS}}$  will not result in excessively high absorption in the DPS section and the absorption losses in the PMC waveguide will also be reduced. Figure 14(b) depicts the value of  $\Delta n_{\text{TE}} - \Delta n_{\text{TM}}$  of the DPS as a function of wavelength with different bias voltages after a 100 nm blueshift by the QWI technique, based on Eq. (4). The change in  $\Delta n_{\text{TE}} - \Delta n_{\text{TM}}$  at  $1.55 \mu\text{m}$  is negative, which means the rotation angle has an opposite direction compared to the as-grown QW. Although the absolute value of

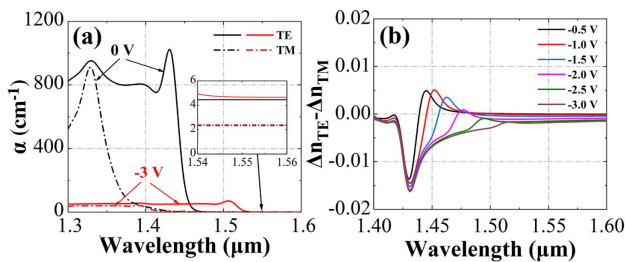


**Fig. 14.** (a) Calculated TE and TM absorption coefficient at  $V_{\text{DPS}} = 0 \text{ V}$  and  $-3 \text{ V}$ , respectively, and (b) value of  $\Delta n_{\text{TE}} - \Delta n_{\text{TM}}$  as a function of wavelength at different bias voltages for a DPS with a 100 nm blueshift using QWI.

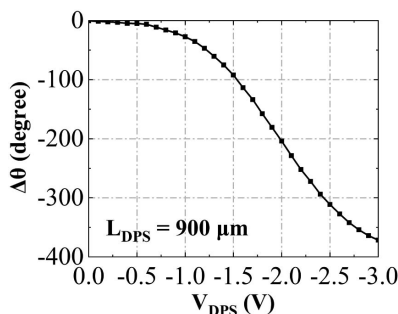


**Fig. 15.** Calculated phase shift angle  $\Delta\theta$  for a  $900 \mu\text{m}$  long DPS with a 100 nm blueshift by QWI at an operating wavelength of  $1.55 \mu\text{m}$ .

$\Delta n_{\text{TE}} - \Delta n_{\text{TM}}$  is lower than for the as-grown QW at  $1.55 \mu\text{m}$ , due to the low absorption the length of the DPS can be extended to increase  $\Delta\theta$  in the DPS. For example, the DPS length could be set to  $900 \mu\text{m}$  when its absorption loss is calculated to be only  $0.21 \text{ dB}$ . The phase shift angle  $\Delta\theta$  as a function of  $V_{\text{DPS}}$  is shown in Fig. 15. A full  $360^\circ$  rotation of the SV can then be achieved when  $V_{\text{DPS}} = -3.0 \text{ V}$ . This result shows that QWI can enhance the performance of DFB-PMC-DPS devices. We note the fabricated PMC length should be kept as close as possible to the designed value by precise control of the cleaving. Here a LOOMIS LSD-100 cleaving tool was used with a cleaving accuracy of  $\pm 1 \mu\text{m}$ . The resulting variation in the PCE is less than  $0.1\%$ , confirming the tool meets the required cleaving tolerance.

## 5. CONCLUSION

We have, for the first time, proposed and fabricated an SWG DFB laser monolithically integrated with a PMC, and an SWG DFB laser monolithically integrated with PMC and DPS based on the IEL PIC scheme. For the  $490 \mu\text{m}$  long PMC devices, a TE/TM conversion efficiency of  $98.4\%$  was obtained over a broad range of  $I_{\text{DFB}}$  from  $140$  to  $190 \text{ mA}$  at a  $1555 \text{ nm}$  operating wavelength. The wavelength dependence was also calculated and measured; the devices have a PCE  $> 90\%$  over the wavelength range of  $1543$  to  $1568 \text{ nm}$ . For DFB-PMC-DPS devices, a rotation of nearly  $60^\circ$  in the SV on the surface of the Poincaré sphere was obtained over a range of bias voltage from  $0$  to  $-3 \text{ V}$  at  $I_{\text{DFB}} = 170 \text{ mA}$ . A major advantage of the design is that only a single MOVPE step and two dry-etch steps are required to fabricate the device, significantly reducing complexity and cost. The demonstrated devices should be useful in realizing various types of polarization-multiplexed coherent transceivers.

**Funding.** Engineering and Physical Sciences Research Council (EP/R042578/1); Chinese Ministry of Education Collaborative Project (B17023).

**Acknowledgment.** We would like to acknowledge the staff of the James Watt Nanofabrication Centre at the University of Glasgow for their help in fabricating the devices.

**Disclosures.** The authors declare no conflicts of interest.

**Data Availability.** Data underlying the results presented in this paper are not publicly available at this time but may be obtained from the authors upon reasonable request.

## REFERENCES

- P. J. Winzer, D. T. Neilson, and A. R. Chraplyvy, "Fiber-optic transmission and networking: the previous 20 and the next 20 years," *Opt. Express* **26**, 24190–24239 (2018).
- S. Ghosh, Y. Kawabata, T. Tanemura, and Y. Nakano, "Polarization-analyzing circuit on InP for integrated Stokes vector receiver," *Opt. Express* **25**, 12303–12310 (2017).
- D. Che and W. Shieh, "Polarization demultiplexing for Stokes vector direct detection," *J. Lightwave Technol.* **34**, 754–760 (2016).



4. B. Holmes, M. Naeem, D. Hutchings, J. Marsh, and A. Kelly, "A semiconductor laser with monolithically integrated dynamic polarization control," *Opt. Express* **20**, 20545–20550 (2012).
5. M. Kazi, S. Ghosh, H. Sodabanlu, K. Suzuki, M. Sugiyama, T. Tanemura, and Y. Nakano, "High-speed carrier-injection-based polarization controller with InGaAlAs/InAlAs multiple-quantum wells," *IEEE Photonics Technol. Lett.* **29**, 1951–1954 (2017).
6. S. I. H. Azzam, N. F. Areed, M. M. Abd-Elrazzak, H. El-Mikati, and S. S. Obayya, "Compact polarization rotator based on SOI platform," in *31st National Radio Science Conference (NRSC)* (IEEE, 2014), pp. 288–293.
7. U. Khalique, Y. Zhu, J. van der Tol, L. Augustin, R. Hanfoug, F. Groen, P. van Veldhoven, M. Smit, M. van de Moosdijk, and W. de Laat, "Ultrashort polarization converter on InP/InGaAsP fabricated by optical lithography," in *Integrated Photonics Research and Applications* (Optica, 2005), paper IWA3.
8. A. E. Elfiqi, R. Kobayashi, R. Tanomura, T. Tanemura, and Y. Nakano, "Fabrication-tolerant half-ridge InP/InGaAsP polarization rotator with etching-stop layer," *IEEE Photonics Technol. Lett.* **32**, 663–666 (2020).
9. M. Ito, K. Okawa, T. Suganuma, T. Fukui, E. Kato, T. Tanemura, and Y. Nakano, "Efficient InGaAsP MQW-based polarization controller without active-passive integration," *Opt. Express* **29**, 10538–10545 (2021).
10. M. A. Naeem and K. Abid, "A novel full polarisation controller integrated monolithically with a semiconductor laser," in *Asia Communications and Photonics Conference* (Optica, 2015), paper AM1A.2.
11. J. Bregenzer, S. McMaster, M. Sorel, B. Holmes, and D. Hutchings, "Polarisation mode converter monolithically integrated within a semiconductor laser," in *Conference on Lasers and Electro-Optics* (Optica, 2008), paper CThM2.
12. A. E. Elfiqi, R. Tanomura, D. Yu, W. Yanwachirakul, H. Shao, Y. Suzuki, T. Tanemura, and Y. Nakano, "Robust InP/InGaAsP polarization rotator based on mode evolution," *IEEE Photonics Technol. Lett.* **34**, 109–112 (2022).
13. X. Sun, W. Cheng, Y. Sun, S. Ye, A. Al-Moathin, Y. Huang, R. Zhang, S. Liang, B. Qiu, J. Xiong, X. Liu, J. H. Marsh, and L. Hou, "Simulation of an AlGaInAs/InP electro-absorption modulator monolithically integrated with sidewall grating distributed feedback laser by quantum well intermixing," *Photonics* **9**, 564 (2022).
14. X. Sun, S. Ye, W. Cheng, S. Liang, Y. Huang, B. Qiu, Z. Li, J. Xiong, X. Liu, J. H. Marsh, and L. Hou, "Monolithically integrated AlGaInAs MQW polarization mode converter using a stepped height ridge waveguide," *IEEE Photonics J.* **14**, 6632606 (2022).
15. T. Tanemura and Y. Nakano, "Compact InP Stokes-vector modulator and receiver circuits for short-reach direct-detection optical links," *IEICE Trans. Electron.* **E101.C**, 594–601 (2018).
16. H. Deng, D. O. Yevick, C. Brooks, and P. E. Jessop, "Design rules for slanted-angle polarization rotators," *J. Lightwave Technol.* **23**, 432–445 (2005).
17. M. Renaud, M. Bachmann, and M. Eрман, "Semiconductor optical space switches," *IEEE J. Sel. Top. Quantum Electron.* **2**, 277–288 (1996).
18. B. L. Weiss, Y. Chan, W. C. Shiu, and E. H. Li, "The electro-optic properties of interdiffused InGaAs/InP quantum well structures," *J. Appl. Phys.* **88**, 3418–3425 (2000).
19. M. Sugawara, T. Fujii, S. Yamazaki, and K. Nakajima, "Theoretical and experimental study of the optical-absorption spectrum of exciton resonance in  $\text{In}_{0.53}\text{Ga}_{0.47}\text{As}/\text{InP}$  quantum wells," *Phys. Rev. B* **42**, 9587–9597 (1990).
20. J. Minch, S. Park, T. Keating, and S. Chuang, "Theory and experiment of InGaAsP and InGaAlAs long-wavelength strained quantum-well lasers," *IEEE J. Quantum Electron.* **35**, 771–782 (1999).
21. L. Hou, M. Tan, M. Haji, I. Eddie, and J. H. Marsh, "EML based on side-wall grating and identical epitaxial layer scheme," *IEEE Photonics Technol. Lett.* **25**, 1169–1172 (2013).
22. M. Razeghi, R. Blondeau, M. Krakowski, J.-C. Bouley, M. Papuchon, B. Cremoux, and J. Duchemin, "Low-threshold distributed feedback lasers fabricated on material grown completely by LP-MOCVD," *IEEE J. Quantum Electron.* **21**, 507–511 (1985).
23. L. Hou, M. Haji, J. Akbar, J. H. Marsh, and A. C. Bryce, "AlGaInAs/InP monolithically integrated DFB laser array," *IEEE J. Quantum Electron.* **48**, 137–143 (2011).